



# High transparent mid-infrared silicon “window” decorated with amorphous photonic structures fabricated by facile phase separation

YAFENG ZHANG,<sup>1</sup> XINHUA HU,<sup>2,4</sup> SHAO-WEI WANG,<sup>1</sup> BO ZHANG,<sup>1,5</sup> LEI SHI,<sup>3</sup> XIAOHAN LIU,<sup>3</sup> JIAN ZI,<sup>3</sup> AND WEI LU<sup>1,\*</sup>

<sup>1</sup>State Key Laboratory of Infrared Physics, Shanghai Institute of Technical Physics, Chinese Academy of Sciences, Shanghai 200083, China

<sup>2</sup>Department of Materials Science, Key Laboratory of Micro- and Nano-Photonic Structures (Ministry of Education), and Laboratory of Advanced Materials, Fudan University, Shanghai 200433, China

<sup>3</sup>Department of Physics, Key Laboratory of Micro and Nano Photonic Structures (MOE) and Key Laboratory of Surface Physics Fudan University, Shanghai 200433, China Collaborative Innovation Center of Advanced Microstructures, Nanjing University, Nanjing 210093, China

<sup>4</sup>huxh@fudan.edu.cn

<sup>5</sup>bozhang@mail.sitp.ac.cn

\*luwei@mail.sitp.ac.cn

**Abstract:** High transparency in the infrared (IR) region is desirable for most common IR materials and devices, due to their high interfacial reflectance, resulting from the high refractive indices of constituent substances. Herein, a new strategy, with using phase-separated polystyrene (PS)/polymethylmethacrylate (PMMA) blends as masks, is proposed to fabricate subwavelength structures for Si with significantly enhanced mid-IR transmission. Maximum transmittance approaching to 70% and 90% are achieved with single and double-side structured Si respectively. The fabricated subwavelength structures are short-range ordered amorphous photonic structures (APSs). By using different spin-coating speeds and molar ratios of PS to PMMA and by adjusting the etching duration time, tunable enhanced transmission are also obtained. The good performance of high transmission is confirmed by mid-IR thermal imaging experiments. Furthermore, the enhanced transmission is effective over a wide range of incident angles up to 50° and well maintained at high temperatures up to 600 °C.

© 2018 Optical Society of America under the terms of the [OSA Open Access Publishing Agreement](#)

**OCIS codes:** (050.6624) Subwavelength structures; (220.4000) Microstructure fabrication; (160.5470) Polymers; (040.6040) Silicon; (300.6340) Spectroscopy, infrared; (120.7000) Transmission.

## References and links

1. P. Klocek, *Handbook of Infrared Optical Materials* (Marcel Dekker, 1991).
2. M. Born and E. Wolf, *Principles of Optics* (Cambridge University, 1999).
3. H. A. Macleod, *Thin-film optical filters* (CRC, 2001).
4. H. K. Raut, V. A. Ganesh, A. S. Nair, and S. Ramakrishna, “Anti-reflective coatings: A critical, in-depth review,” *Energy Environ. Sci.* **4**(10), 3779–3804 (2011).
5. Y. Q. Pan, L. X. Hang, Z. S. Wu, and Y. B. Yin, “Design and fabrication of ultra broadband infrared antireflection hard coatings on ZnSe in the range from 2 to 16 μm,” *Infrared Phys. Technol.* **52**(5), 193–195 (2009).
6. R. Z. Moghadam, H. Ahmadvand, and M. Jannesari, “Design and fabrication of multi-layers infrared antireflection coating consisting of ZnS and Ge on ZnS substrate,” *Infrared Phys. Technol.* **75**, 18–21 (2016).
7. A. Szeghalmi, M. Helgert, R. Brunner, F. Heyroth, U. Gösele, and M. Knez, “Atomic layer deposition of Al<sub>2</sub>O<sub>3</sub> and TiO<sub>2</sub> multilayers for applications as bandpass filters and antireflection coatings,” *Appl. Opt.* **48**(9), 1727–1732 (2009).
8. B. M. Wang, J. S. Price, and N. C. Giebink, “Durable broadband ultralow index fluoropolymer antireflection coatings for plastic optics,” *Optica* **4**(2), 239–242 (2017).

9. J. Q. Xi, M. F. Schubert, J. K. Kim, E. F. Schubert, M. F. Chen, S. Y. Lin, W. Liu, and J. A. Smart, "Optical thin-film materials with low refractive index for broadband elimination of Fresnel reflection," *Nat. Photonics* **1**(3), 176–179 (2007).
10. X. X. Zhang, S. Cai, D. You, L. H. Yan, H. B. Lv, X. D. Yuan, and B. Jiang, "Template-free sol-gel preparation of superhydrophobic ormosil films for double-wavelength broadband antireflective coatings," *Adv. Funct. Mater.* **23**(35), 4361–4365 (2013).
11. A. Yildirim, T. Khudiyev, B. Daglar, H. Budunoglu, A. K. Okyay, and M. Bayindir, "Superhydrophobic and omnidirectional antireflective surfaces from nanostructured ormosil colloids," *ACS Appl. Mater. Interfaces* **5**(3), 853–860 (2013).
12. S. Walheim, E. Schäffer, J. Mlynek, and U. Steiner, "Nanophase-separated polymer films as high-performance antireflection coatings," *Science* **283**(5401), 520–522 (1999).
13. W. Joo, M. S. Park, and J. K. Kim, "Block copolymer film with sponge-like nanoporous structure for antireflection coating," *Langmuir* **22**(19), 7960–7963 (2006).
14. X. Li, J. P. Gao, L. J. Xue, and Y. C. Han, "Porous polymer films with gradient-refractive-index structure for broadband and omnidirectional antireflection coatings," *Adv. Funct. Mater.* **20**(2), 259–265 (2010).
15. X. Li, X. H. Yu, and Y. C. Han, "Polymer thin films for antireflection coatings," *J. Mater. Chem. C Mater. Opt. Electron. Devices* **1**(12), 2266–2285 (2013).
16. D. M. Sim, M. J. Choi, Y. H. Hur, B. Nam, G. Chae, J. H. Park, and Y. S. Jung, "Ultra-high optical transparency of robust, graded-index, and anti-fogging silica coating derived from Si-containing block copolymers," *Adv. Opt. Mater.* **1**(6), 428–433 (2013).
17. C. G. Bernhard, "Structural and functional adaptation in a visual system," *Endeavour* **26**, 79–84 (1967).
18. D. H. Raguin and G. M. Morris, "Antireflection structured surfaces for the infrared spectral region," *Appl. Opt.* **32**(7), 1154–1167 (1993).
19. D. G. Stavenga, S. Foletti, G. Palasantzas, and K. Arikawa, "Light on the moth-eye corneal nipple array of butterflies," *Proc. Biol. Sci.* **273**(1587), 661–667 (2006).
20. S. A. Boden and D. M. Bagnall, "Tunable reflection minima of nanostructured antireflective surfaces," *Appl. Phys. Lett.* **93**(13), 133108 (2008).
21. P. B. Clapham and M. C. Hutley, "Reduction of lens reflexion by the "Moth Eye" principle," *Nature* **244**(5414), 281–282 (1973).
22. K. Hadobás, S. Kirsch, A. Carl, M. Acet, and E. F. Wassermann, "Reflection properties of nanostructure-arrayed silicon surfaces," *Nanotechnology* **11**(3), 161–164 (2000).
23. J. Zhu, Z. Yu, G. F. Burkhard, C.-M. Hsu, S. T. Connor, Y. Xu, Q. Wang, M. McGehee, S. Fan, and Y. Cui, "Optical absorption enhancement in amorphous silicon nanowire and nanocone arrays," *Nano Lett.* **9**(1), 279–282 (2009).
24. W.-L. Min, B. Jiang, and P. Jiang, "Bioinspired self-cleaning antireflection coatings," *Adv. Mater.* **20**(20), 3914–3918 (2008).
25. P. Kothary, B. M. Phillips, S.-Y. Leo, and P. Jiang, "Bioinspired broadband midwavelength infrared antireflection coatings on silicon," *J. Vac. Sci. Technol. B* **34**(4), 041807 (2016).
26. S. Ji, J. Park, and H. Lim, "Improved antireflection properties of moth eye mimicking nanopillars on transparent glass: flat antireflection and color tuning," *Nanoscale* **4**(15), 4603–4610 (2012).
27. Y. Ou, X. Zhu, V. Jokubavicius, R. Yakimova, N. A. Mortensen, M. Syväjärvi, S. Xiao, and H. Ou, "Broadband antireflection and light extraction enhancement in fluorescent SiC with nanodome structures," *Sci. Rep.* **4**(1), 4662 (2014).
28. Q. Chen, G. Hubbard, P. A. Shields, C. Liu, D. W. E. Allsopp, W. N. Wang, and S. Abbott, "Broadband moth-eye antireflection coatings fabricated by low-cost nanoimprinting," *Appl. Phys. Lett.* **94**(26), 263118 (2009).
29. H. K. Raut, S. S. Dinachali, Y. C. Loke, R. Ganesan, K. K. Ansah-Antwi, A. Góra, E. H. Khoo, V. A. Ganesh, M. S. M. Saifullah, and S. Ramakrishna, "Multiscale ommatidial arrays with broadband and omnidirectional antireflection and antifogging properties by sacrificial layer mediated nanoimprinting," *ACS Nano* **9**(2), 1305–1314 (2015).
30. G. J. Tan, J.-H. Lee, Y.-H. Lan, M.-K. Wei, L.-H. Peng, I.-C. Cheng, and S.-T. Wu, "Broadband antireflection film with moth-eye-like structure for flexible display applications," *Optica* **4**(7), 678–683 (2017).
31. L. Shi, Y. Zhang, B. Dong, T. Zhan, X. Liu, and J. Zi, "Amorphous photonic crystals with only short-range order," *Adv. Mater.* **25**(37), 5314–5320 (2013).
32. B. Q. Dong, T. R. Zhan, X. H. Liu, L. P. Jiang, F. Liu, X. H. Hu, and J. Zi, "Optical response of a disordered bicontinuous macroporous structure in the longhorn beetle *Sphingnotus mirabilis*," *Phys. Rev. E Stat. Nonlin. Soft Matter Phys.* **84**(1), 011915 (2011).
33. J. W. Cahn and J. E. Hilliard, "Free energy of a nonuniform system. I. Interfacial free energy," *J. Chem. Phys.* **28**(2), 258–267 (1958).
34. J. Zhu, L.-Q. Chen, J. Shen, and V. Tikare, "Coarsening kinetics from a variable-mobility Cahn-Hilliard equation: application of a semi-implicit Fourier spectral method," *Phys. Rev. E Stat. Phys. Plasmas Fluids Relat. Interdiscip. Topics* **60**(4 Pt A), 3564–3572 (1999).
35. K. Tanaka, A. Takahara, and T. Kajiyama, "Film thickness dependence of the surface structure of immiscible polystyrene/poly (methyl methacrylate) blends," *Macromolecules* **29**(9), 3232–3239 (1996).
36. S. Walheim, M. Böltau, J. Mlynek, G. Krausch, and U. Steiner, "Structure formation via polymer demixing in spin-cast films," *Macromolecules* **30**(17), 4995–5003 (1997).

37. M. Ibn-Elhaj and M. Schadt, "Optical polymer thin films with isotropic and anisotropic nano-corrugated surface topologies," *Nature* **410**(6830), 796–799 (2001).
38. A. Cadby, R. Dean, A. M. Fox, R. A. L. Jones, and D. G. Lidzey, "Mapping the fluorescence decay lifetime of a conjugated polymer in a phase-separated blend using a scanning near-field optical microscope," *Nano Lett.* **5**(11), 2232–2237 (2005).
39. Y. G. Liao, Z. H. Su, X. G. Ye, Y. Q. Li, J. C. You, T. F. Shi, and L. J. An, "Kinetics of surface phase separation for PMMA/SAN thin films studied by in situ atomic force microscopy," *Macromolecules* **38**(2), 211–215 (2005).
40. L. Fang, M. Wei, C. Barry, and J. Mead, "Effect of spin speed and solution concentration on the directed assembly of polymer blends," *Macromolecules* **43**(23), 9747–9753 (2010).
41. S. Ebbens, R. Hodgkinson, A. J. Parnell, A. Dunbar, S. J. Martin, P. D. Topham, N. Clarke, and J. R. Howse, "In Situ imaging and height reconstruction of phase separation processes in polymer blends during spin coating," *ACS Nano* **5**(6), 5124–5131 (2011).
42. S. Harirchian-Saei, M. C. Wang, B. D. Gates, and M. G. Moffitt, "Directed polystyrene/poly(methyl methacrylate) phase separation and nanoparticle ordering on transparent chemically patterned substrates," *Langmuir* **28**(29), 10838–10848 (2012).
43. H. Zhang and S. Takeoka, "Morphological evolution within spin-cast ultrathin polymer blend films clarified by a freestanding method," *Macromolecules* **45**(10), 4315–4321 (2012).
44. L. Robeson, "Historical perspective of advances in the science and technology of polymer blends," *Polymers (Basel)* **6**(5), 1251–1265 (2014).
45. W. Vogel, *Glass Chemistry* (Springer, 1994).
46. J. Erlebacher, M. J. Aziz, A. Karma, N. Dimitrov, and K. Sieradzki, "Evolution of nanoporosity in dealloying," *Nature* **410**(6827), 450–453 (2001).
47. J. C. Maxwell Garnett, "Colours in Metal Glasses and in Metallic Films," *Philos. Trans. R. Soc. Lond.* **203**(359-371), 385–420 (1904).
48. T. C. Choy, *Effective Medium Theory: Principles and Applications* (Oxford University, 1999).
49. Z. Q. Xiong, F. Y. Zhao, J. Yang, and X. H. Hu, "Comparison of optical absorption in Si nanowire and nanoporous Si structures for photovoltaic applications," *Appl. Phys. Lett.* **96**(18), 181903 (2010).
50. E. D. Palik, ed., *Handbook of Optical Constants of Solids* (Academic, 1985).
51. J. Zi, J. Wan, and C. Zhang, "Large frequency range of negligible transmission in one-dimensional photonic quantum well structures," *Appl. Phys. Lett.* **73**(15), 2084–2086 (1998).
52. Z. M. Zhang, L. M. Hanssen, and R. U. Datla, "Polarization-dependent angular reflectance of silicon and germanium in the infrared," *Infrared Phys. Technol.* **37**(4), 539–546 (1996).

## 1. Introduction

When a plane wave of light is incident on an interface between two different media, reflection always appears because of the refractive index (impedance) mismatch. In the mid-IR region, due to the high refractive indices for most of IR materials, the reflectance could achieve as high as 40% [1]. This will greatly influence the performance of corresponding IR devices such as IR lenses, IR cameras and IR photodetectors. In order to reduce the reflection and enhance the transmission, normally, low-refractive-index layers are applied to coat the IR devices. The underlying physics is index (impedance) matching and destructive interference. To maximize the transmission, three requirements should be satisfied. First, the coating layer should have a refractive index  $n_c = \sqrt{n_0 \cdot n_s}$  with  $n_0$  and  $n_s$  being the indices of the background medium (air) and IR material, respectively. Second, the thickness of coating layer need to be a quarter of the wavelength in the coating [2]. Finally, the coating film should possess a negligible value in the imaginary part of the refractive index, so that it is transparent and does not absorb light in the IR region.

Two main approaches have been adopted to obtain low-refractive-index layers: thin-film coatings [3] and subwavelength photonic structures [4]. Thin-film coatings of a homogeneous layer or heterogeneous layers have been realized by techniques such as thermal or electron beam deposition [5,6], atomic layer deposition [7], oblique-angle deposition [8,9] and sol-gel process [10,11]. The coating materials can be natural ones, polymer blend or modified block-copolymer [12–16]. This approach facilitates the fabrication of large-area antireflection layers, while its limitation is that appropriate coating media are unavailable in some wavelength ranges. In addition, the use of coating materials may bring problems such as low thermostabilization, low adhesion and inconsistent stabilities in extreme environments.

Subwavelength photonic structures, represented by the famous moth-eye structure [17], effectively possess low refractive indices and thus can reduce reflection and enhance

transmission. Since no coating material is needed in subwavelength structures, the troublesome problems in thin-film coatings can be avoided [18,19]. Moreover, wide-angle antireflection and transmission can be achieved by using the subwavelength structures, which is quite useful in practical applications. Artificial subwavelength photonic structures have been fabricated by various methods. These methods commonly consist of two processes: fabricating subwavelength masks and transferring mask patterns to the substrates by using conventional etching techniques [4]. Currently, subwavelength masks at mid-IR region are mainly obtained by several techniques: forming patterns by electron beam lithography (EBL) [20] or interference lithography (IL) [21,22], and obtaining templates prepared by self-assembly of monolayer colloidal spheres [23–28] or by nanoimprint technique [28–30]. These techniques suffer from some apparent drawbacks, such as limited mass-productive ability for EBL, advanced equipment requirements for generating submicron patterns by IL, time consuming and limited tunability in self-assembly of colloidal spheres, and rigid masks required in nanoimprint technique. All these issues greatly limit the potential practical applications of subwavelength photonic structures.

Here, a new strategy, by using facile phase separation of polymer blends as masks, is firstly proposed to fabricate subwavelength photonic structures on IR materials (Si) for enhanced transmission. The whole fabrication process is simple, tunable, mass-productive and it only uses well-established processing techniques [See Fig. 1(a)]. The fabricated subwavelength structures are found to possess only short-range orders, called amorphous photonic structures (APSSs) [31,32]. By adjusting fabrication parameters including molar ratios of polymer blends, spin-coating speeds and etching duration time, tunable low effective refractive indices and thus the enhanced transmission are obtained by the subwavelength structures. Hence, tunable high transparent “window” can be achieved for IR materials. The enhanced transmission can be effective in a wide range of incident angles due to the subwavelength characteristic. The proposed strategy here can also be applied to other IR materials and devices, such as Ge lenses, IR cameras and IR photodetectors.

## 2. Results and discussions

### 2.1 Fabrication of Si subwavelength photonic structures

Phase separation of polymer blends has been extensively studied theoretically and experimentally, due to their potential applications in photovoltaic devices, light-emitting diodes, antireflection coatings and biological devices [12, 29, 30, 33–43]. Furthermore, when one phase is removed from the blends, various nano- and microporous structures are readily obtained and they can serve as templates for novel applications. In this paper, phase separation is used to fabricate subwavelength photonic structures for enhancing transmission through IR materials.

The whole fabrication process is schematically illustrated in Fig. 1(a). First, a blend of PS and PMMA is dissolved in tetrahydrofuran (THF), and the solution is cast on a pre-cleaned IR substrate (here is a Si wafer) by the well-established spin-coating technique. Because of the immiscibility of PS/PMMA and highly volatile characteristic of THF, a large-area phase-separated thin film is formed in tens of seconds during the spin-coating process. Then, the sample is immersed into acetic acid, so that the PMMA phase is removed and a patterned PS phase is left [Fig. 1(b)].

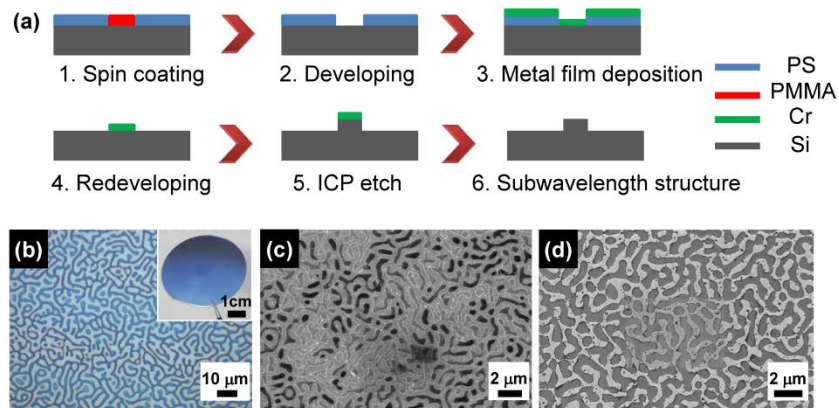


Fig. 1. (a) Schematic illustration of the process of fabricating Si subwavelength structures, in which phase-separated PS/PMMA blends are used as masks. (b) Optical microscopic image of phase-separated PS pattern after the developing process in (a). Inset is the optical image of a 2-inch Si wafer covered with the phase-separated PS film. (c) SEM image of chromium-coated phase-separated PS pattern after the metal-film-deposition process in (a). (d) SEM image of phase-separated chromium pattern after the redeveloping process in (a), which will be used as the masks for the following ICP-etch process. The PS/PMMA blend in (b)-(d) was prepared by using a molar ratio 1:1 of PS to PMMA and a spin-coating speed of 5000 rpm.

Thicknesses of the phase-separated PS films range from 60 nm to 120 nm [Fig. 8 in the Appendix], which depends on both the concentration of polymer blends in solutions and the spin-coating speed. Porous polymer films have been used directly as antireflection coatings in the visible region [12,37], but they cannot work in the IR range, due to their thin thickness and large loss for IR light.

The structured PS film here cannot be used directly as masks for etching since it is not thick enough to be depleted in dry etching process. A 5 nm-thick chromium (Cr) film is thus deposited on the porous PS film and then the sample is immersed into cyclohexane, so that the Cr-coated PS parts are removed and a complementary patterned Cr hard mask is formed. After a dry etching, the sample is immersed into Cr etchant to remove the Cr masks. A Si subwavelength photonic structure is finally obtained on the Si wafer.

Figure 1(b) illustrates the microscopic optical image of a structured PS film. The structured PS film is fabricated on a 2-inch Si wafer and shows a uniform light-blue color [Inset in Fig. 1(b)], indicating the mass-productive capacity of the strategy. The conformal deposition of thin Cr layer on the structured PS film [Fig. 1(c)] ensures good complementary preparation of Cr hard masks [Fig. 1(d)].

## 2.2 Si subwavelength structures of different thicknesses with enhanced mid-IR transmission by varying the etching duration time

The Si wafers coated with the above structured Cr films were etched by standard inductively coupled plasma reactive ion etching (ICP-RIE) processes. By varying the etching duration time, Si subwavelength structures with different thicknesses were fabricated on the Si wafers. Several parameters, such as reactive ions density, substrate temperatures and opening sizes of masks, can influence the etching rate. In our experiments, the etching rate is estimated to be about 500 nm/min.

Figure 2(a) shows the obtained large-area Si structure, which is uniform and has no obvious cracks. A connected type of disordered porous structure is formed at the surface of Si wafer [Fig. 2(b)]. Here, the used mask is prepared under the condition of a molar ratio 1:1 of PS to PMMA and a spin-coating speed of 5000 rpm. The Si structure has smooth sidewalls with profile angle about 85 degree, as can be observed from oblique and cross-sectional scanning-electron-microscopy (SEM) images [Figs. 2(c) and 2(d)]. The structured Si surface

also shows a vivid color, due to the interference effect [Inset in Fig. 2(a) for a sample etched for 2 min]. Such a structural color is uniform in a large area, confirming the uniformity of the fabricated Si structures.

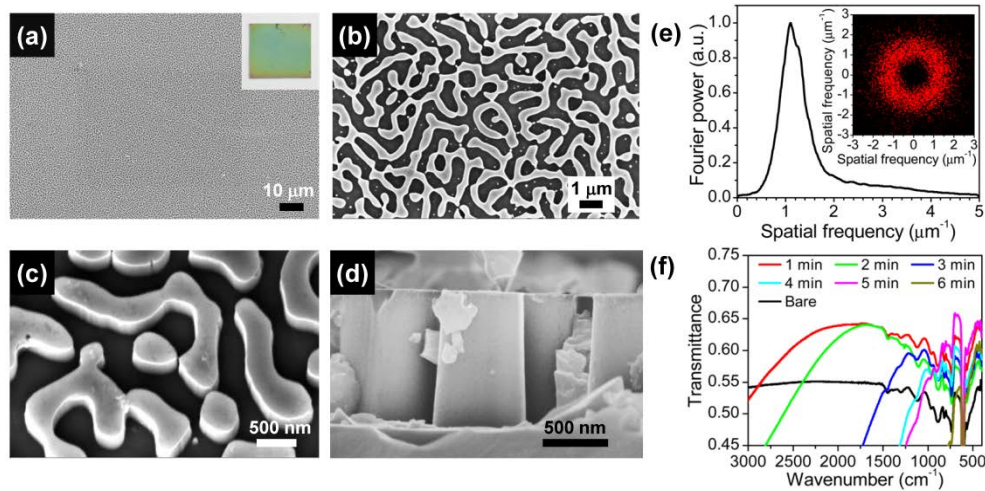


Fig. 2. (a) SEM image of the fabricated large-area Si subwavelength structure and (b) its enlarged view. Inset in (a) is the optical image of the sample. (c) Oblique and (d) cross-sectional SEM images of the structure in (b). (e) Rationally averaged Fourier transform spectrum for the structure in (a). Inset in (e) is the corresponding two-dimensional Fourier transform spectrum. (f) Transmission spectra of the fabricated single-side structured Si samples with different etching duration time. The transmission spectrum of a double-side polished Si wafer was shown for comparison (black line). The sample in (a-d) was fabricated under the condition of a molar ratio 1:1 of PS to PMMA, a spin-coating speed of 5000 rpm and etching duration time for 2 min.

The porous structure in Fig. 2(a) was further analyzed by doing 2D fast Fourier transform (FFT) [Fig. 2(e)]. A ring pattern can be seen in the 2D Fourier transform power spectrum [Inset in Fig. 2(e)]. This indicates that the Si porous structure has only a short-range order and thus is a APS. The characteristic length scale  $\Lambda$  of the structure, inverse to the spatial frequency of the scattering peak in rotational averaged FFT spectrum [32], is found to be about 901 nm. Such a structure can be considered as a subwavelength photonic structure for wavelengths  $\lambda_0 > n \cdot \Lambda$  which  $\lambda_0$  is the wavelength in vacuum and  $n$  is the refractive index of substrate ( $n \approx 3.42$  for Si in the IR range) [18]. Since such a structure has a smaller effective refractive index than Si, it can enhance the transmission for light with  $\lambda_0 > n \cdot \Lambda$ .

Figure 2(f) illustrates the transmission spectra for single-side structured Si wafers fabricated with different etching duration time. For comparison, the result of a double-side polished Si wafer is also shown. As can be seen, the maximum transmittance increment is about 10% for these samples, compared to the polished Si wafer. By increasing the etching duration time, the peak wavelength corresponding to maximum transmittance also increases, agreeing well with theoretical expectation.

### 2.3 Tuning the characteristic lengths of subwavelength structures by varying the spin-coating speed

A series of masks were fabricated by varying the spin-coating speeds when keeping the molar ratio of PS to PMMA fixed. The prepared masks with the ratio of 1:1 are shown in Fig. 9 in the Appendix. We can see that the masks exhibit similar morphologies of connected type, but they possess different characteristic lengths. Using such masks, Si subwavelength structures with different characteristic lengths were then fabricated at the surfaces of Si wafers [Figs. 3(a)-3(d) and Figs. 10(a)-10(f) in the Appendix]. From Fourier transform analyses, the

characteristic length is found to decrease with increasing the spin-coating speed [Fig. 3(e) and Fig. 10(g) in the Appendix]. For spin-coating speeds of 1000 rpm, 3000 rpm, 6000 rpm and 8000 rpm, the characteristic lengths are 2090 nm, 976 nm, 856 nm and 747 nm, respectively.

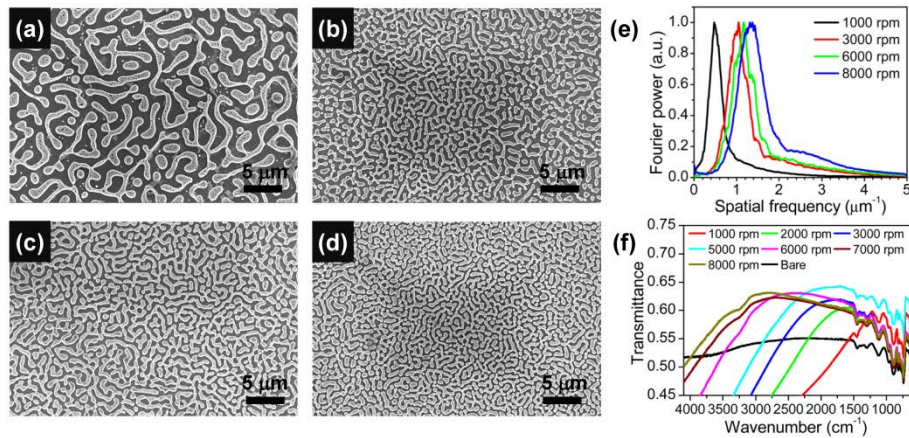


Fig. 3. (a)-(d) SEM images of Si subwavelength structures fabricated by using masks prepared at four different spin-coating speeds: (a) 1000 rpm, (b) 3000 rpm, (c) 6000 rpm and (d) 8000 rpm. (e) Rationally averaged Fourier transform spectra for the structures in (a)-(d). (f) Transmission spectra of the fabricated single-side structured Si samples by using masks prepared at different spin-coating speeds (from 1000 to 8000 rpm). The molar ratio of PS to PMMA 1:1 was used for these samples and the etching duration time was fixed at 1 min.

Figure 3(f) illustrates the transmission spectra for the fabricated samples of single-side structured Si wafers. The spin-coating speeds range from 1000 to 8000 rpm, and the etching duration time is fixed as 1 min. It can be seen that compared with a polished Si wafer, the samples exhibit higher transmission in the mid-IR region. The transmittance increase can be as high as 10% at certain (peak) wavelengths. Moreover, it is found that the etching rate is also strongly related with the characteristic length of the mask. A small etching rate occurs for a small characteristic length, which is also verified by direct SEM observations [Fig. 11 in the Appendix].

#### 2.4 Optimizing the transmittance by varying the molar ratio of PS to PMMA

Optimal transmittance has not been achieved in the above investigations since the molar ratio of PS to PMMA is fixed to be 1:1. In order to further improve the transmittance, more samples were fabricated by varying the molar ratio of PS to PMMA.

Generally, a homogeneous system, consisting of two kinds of polymers in a solution, can be separated into two distinct phases by fast solvent evaporation [Fig. 4(a)] [44]. When the two polymers have close molar concentrations, the process is dominated by spinodal decomposition, resulting in a bicontinuous structure [middle panel in Fig. 4(b)]. In contrast, if one polymer dominates in the blend, droplet-like structures occur due to the process of nucleation and growth [left and right panels in Fig. 4(b)]. By numerically solving the Cahn-Hilliard equations [33,34], the phase-separated structures can be obtained for different ratios of the two polymers. Under the guidance of the theory, similar phase-separated patterns were also experimentally realized in the PS films and Cr masks [Fig. 4(c)].

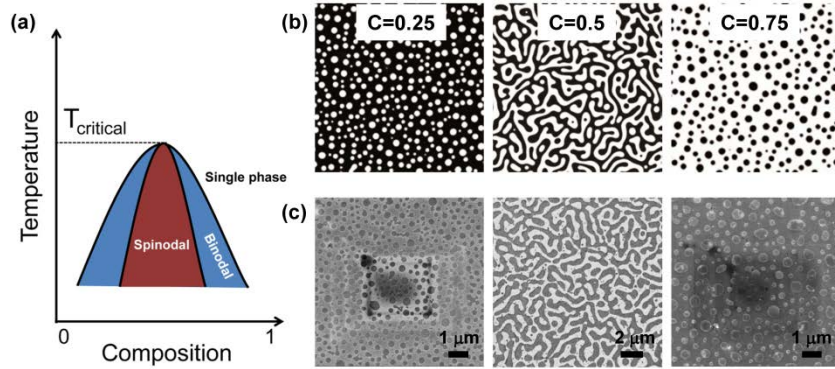


Fig. 4. (a) The schematic phase diagram for binary polymer blend. (b) Numerically generated phase-separated patterns for binary polymer blends with three different ratios, where C is the ratio of one polymer in the blend. (c) SEM images of fabricated phase-separated chromium patterns by using three different molar ratios of PS to PMMA.

Figures 5(a)-5(h) and Fig. 12 in the Appendix illustrate the Si subwavelength structures fabricated by using different molar ratios of PS to PMMA. The spin-coating speed is 5000 rpm and the etching duration time is 2 min. It can be seen that different Si subwavelength patterns, such as holey structures, rod arrays, intermediate continuous and rod-elongated structures, can be obtained. These 2D structures can be fine tuned and resemble the phase-separated structures in metal alloys, glasses and some longhorn beetles [45,46].

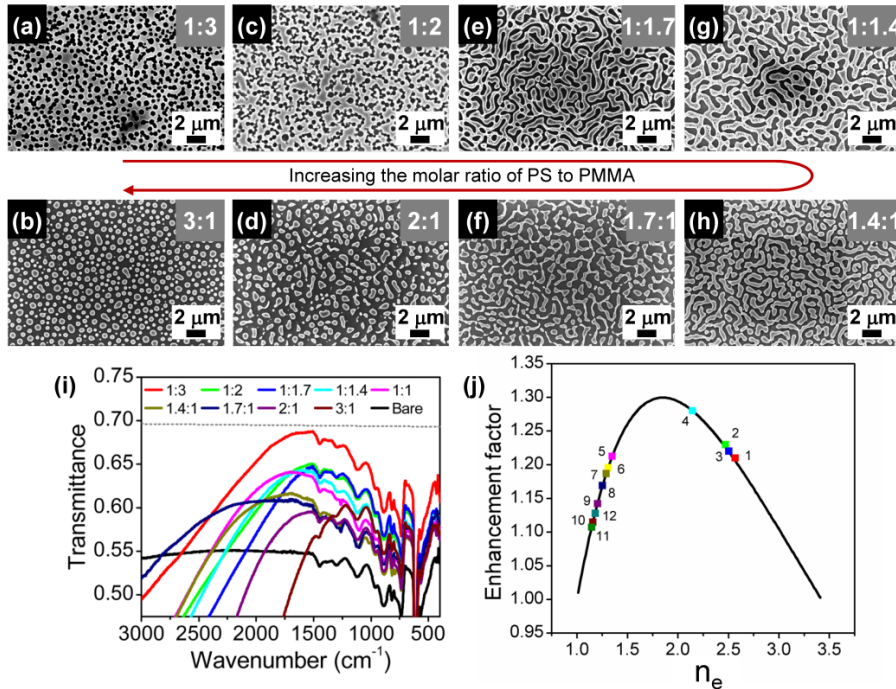


Fig. 5. (a)-(h) SEM images of Si subwavelength structures fabricated by using masks prepared with eight different molar ratios of PS to PMMA. The molar ratios are shown at the upper-right corners of the images. (i) Transmission spectra for the single-side structured samples in (a)-(h). The ideal maximum transmittance of 70% is also shown for comparison (the gray dot line). (j) Effective refractive indices retrieved for twelve samples. Sample markers 1-12 represent the samples fabricated with molar ratios of PS to PMMA of 1:6, 1:5, 1:4, 1:3, 1:2, 1:1.7, 1:1.4, 1:1, 1.4:1, 1.7:1, 2:1, 3:1, respectively.

Transmission spectra were measured for the samples of single-side structured Si wafers, as shown in Fig. 5(i) and Fig. 13(a) in the Appendix. We can see that the transmission is enhanced in the mid-IR region. The heights and positions of the transmission peaks are found to be different for these samples. When the molar ratio of PS to PMMA is 1:3, the maximal transmittance of 69% is obtained, very close to the ideal value of 70% (obtained by substituting  $T_1 = 1$  and  $R_1 = 0$  in Eq. (1) in the Appendix).

The subwavelength photonic structure can be regarded as a low-refractive-index layer with a refractive index  $n_e$  and thickness  $t_e$ , which is coated on a Si wafer with a refractive index  $n_{Si}$ . Based on a transfer-matrix method, the relationship between the transmittance enhancement and  $n_e$  can be obtained [Eq. (1) in the Appendix], as shown as the black curve in Fig. 5(j). Different samples exhibit different values in the heights and positions of transmission enhancement peaks [Fig. 13(b) in the Appendix]. The heights of transmission enhancement peaks are plotted as symbols in Fig. 5(j). Thus, the effective refractive indices can be obtained for different samples. It can be seen that the effective refractive indices range from 1.18 to 2.57. For the sample with the maximal measured transmission of 69%, the effective refractive index is 2.1, close to the ideal value 1.85 for perfect transmission. Here, the effective refractive index  $n_e$  is lower than  $n_{Si}$  due to the existence of air holes, which can also be simply understood by conventional effective medium theory [47,48]. The thicknesses of subwavelength structures can also be retrieved by using the wavelengths of transmission peaks [Fig. 14(a) in the Appendix]. For our samples here, the thicknesses range from 0.80 to 1.76  $\mu\text{m}$ , which is consistent with our experimental observations [Figs. 14(b)-14(d) in the Appendix]. Note that the experimental measured values based on SEM images are slightly lower than those theoretical ones. It may lie on that the absorption of materials is not included in the calculations.

### 2.5 Cutoff wavelengths of enhanced transmission for the subwavelength structures

The fabricated Si APS layers can enhance the transmission through Si wafers in a broad mid-IR region. Nevertheless, when the incident wavelength is shorter than the cutoff wavelength, such an enhancement effect does not exist and the Si wafers with structured surfaces exhibits lower transmittance than a polished Si wafer [Fig. 2(f), Fig. 3(f) and Fig. 5(i)]. The reason lies on that short-wavelength light is scattered by the Si surface structure and a part of the transmitted light propagates in directions different from the incident one.

The experimental results in previous sections show that the cutoff wavelengths depend on the fabrication conditions and vary in a large range. When the same mask is applied, the cutoff wavelength increases with increasing the etching duration time [Fig. 2(f)], since stronger scattering occurs with increasing the structured layer thickness. For the same molar ratio of PS to PMMA, decreasing the spin-coating speed which produces a longer characteristic length for the structured layer, will increase the cutoff wavelength [Fig. 3(f)]. If both the spin-coating speed and etching duration time are fixed, a complex relationship exists between the cutoff wavelength and the molar ratio of PS to PMMA [Fig. 5(i)], because the characteristic length, the filling ratio of Si and the thickness for the structured layer vary with increasing the molar ratio of PS to PMMA.

In order to obtain a rule for estimating the cutoff wavelength, the transmission spectra are replotted with the wavenumber renormalized by the wavenumbers of transmission peaks [Fig. 15 in the Appendix]. It can be seen that the ratios of cutoff wavenumber to peak wavenumber range from 1.44 to 1.64 in Fig. 2(f), from 1.38 to 1.66 in Fig. 3(f) and from 1.36 to 1.76 in Fig. 5(i). The average of the ratios is about 1.5. Therefore, for our samples, the cutoff wavelength can be estimated as about 0.67 times of the wavelength of transmission peak.

## 2.6. High transparent mid-IR Si “window” through the double-side subwavelength structures and the wide angle and high temperature properties

Double-side Si subwavelength structures can be readily obtained by repeating the fabrication steps on double sides of a polished Si wafer. Figure 6(a) shows the transmission spectrum for the fabricated double-side structured sample using the same fabrication condition as the one in Fig. 5(a). The maximal transmittance of 89% at the peak wavenumber is obtained. Cross-sectional SEM images for the double sides of the structured Si wafer are shown in Fig. 6(b). In order to check the actual performance, the double-side structured Si sample is placed on a steadily working radiator, and the mid-IR thermal images of the radiator are taken. Figure 6(c) shows the IR thermal image of the radiator without any covers and inset is its optical image. Figure 6(d) shows the IR thermal image of the radiator covered with a double-side structured Si sample, and inset is their optical image. A double-side polished Si wafer is also laid aside for comparison. It is obvious that both the symbol markers and radiator ridges below the double-side structured Si sample are clearly observed, while nearly all the features of radiator below the polished Si wafer are lost. This result intuitively shows the high mid-IR transmittance of the double-side structured Si sample.

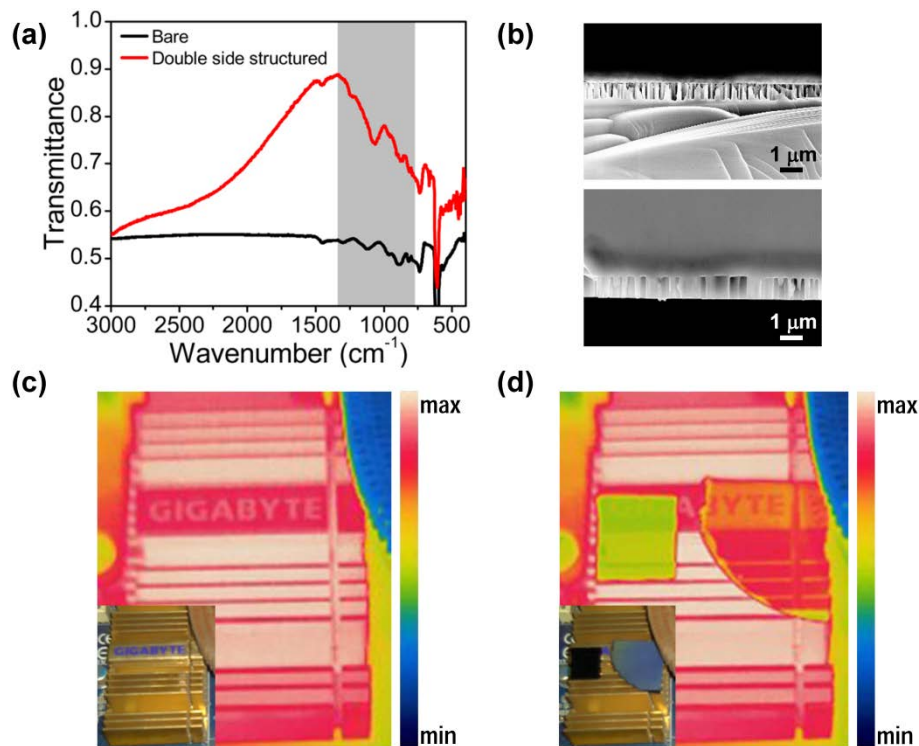


Fig. 6. (a) Transmission spectrum of the double-side structured Si wafer. Each side structure was fabricated by using the same condition as the one in Fig. 5(a). (b) Cross-sectional SEM images for the two sides of the structured Si wafer. (c) Mid-IR thermal image of a working radiator. Inset is its optical image. (d) Mid-IR thermal image for a double-sided polished (left, rectangular) and the double-sided structured (right, sectorial) Si wafer in Fig. (a) on the working radiator. Inset is the optical image. The gray area in (a) is the spectral range of the used IR thermal camera.

The wavelength of enhanced transmission here is nearly independent on the incident angle. Figure 7(a) shows the angle-resolved mid-IR transmission spectra for the double-side structured Si samples. The enhanced transmission is still valid over a large range of angles of incidence, to about  $50^\circ$ , while keeping the spectral ranges and transmittance nearly

unchanged. This wide-angle characteristic is very useful in practical multi-angle imaging applications.

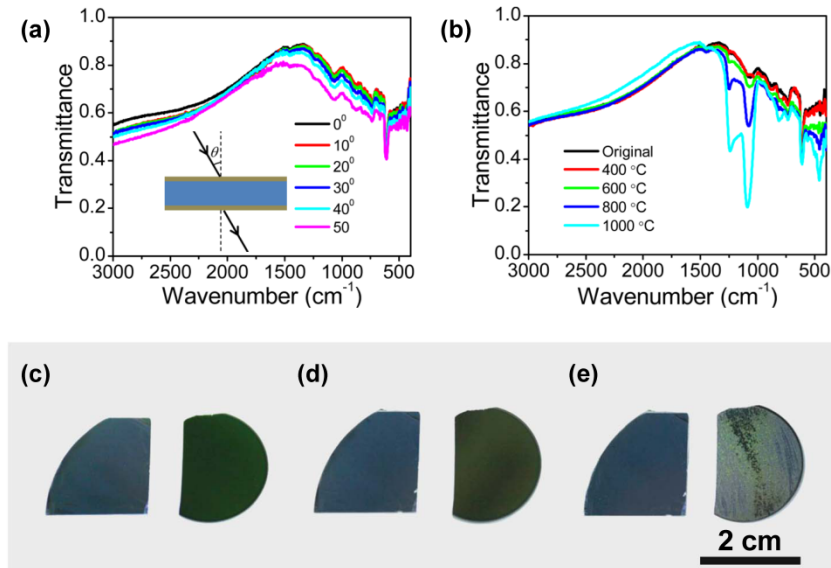


Fig. 7. (a) Angle resolved IR transmission spectra for the double-side structured Si sample in Fig. 6. (b) The IR transmission spectra for the same sample processed at different high temperatures. (c)-(e) Optical images of the fabricated subwavelength structured Si samples (left in each image) processed at different temperatures: (c) Original, (d) 400 °C and (e) 600 °C. The commercial 3-5  $\mu\text{m}$  coated Si (right in each image) IR window (Edmund Optics, 68-524) processed at the same temperatures are also shown for comparison.

Since IR thermal imaging is widely used in high temperature occasions, the enhanced transmission measurements for the fabricated samples processed under different high temperatures were also performed. Figure 7(b) shows that the enhanced transmission are well maintained up to 600 °C. For higher temperatures, Si-O band absorption as well as lattice absorption valleys caused by oxidation and melting effects respectively, are intensified. In spite of this, enhanced transmission still holds in the IR-transparent spectra regions of Si. Figures 7(c)-7(e) show the optical images of the fabricated subwavelength structured Si samples processed at different temperatures (Original, 400 °C and 600 °C), indicating the good high-temperature stability. Commercial 3-5  $\mu\text{m}$  coated Si IR window (Edmund Optics, 68-524) processed under high temperatures are also compared [right in Figs. 7(c)-7(e)] and it is obviously damaged at 600 °C.

### 3. Conclusion

We have proposed and demonstrated a new strategy, with using phase-separated PS/PMMA blends as masks, to fabricate subwavelength surface structures for Si with significantly enhanced mid-IR transmission. The subwavelength structures are APSs with short-range orders. By adjusting parameters in the fabrication process, including molar ratios of PS to PMMA, spin-coating speeds and etching duration time, unique phase-separated Si structures and tunable enhanced transmission in mid-IR region were obtained. Maximum transmittance approaching to the ideal 70% is realized for single-side structured Si wafer. For double-side structured Si, the maximum transmittance can reach 89%. Based on a transfer-matrix method, effective refractive indices were retrieved for the subwavelength structures. It is also found that the cutoff wavelengths of enhanced transmission rely on the characteristic lengths and thicknesses of the fabricated structures, and they are around 0.67 times of the wavelengths of transmission peaks. From the application point of view, the enhanced transmission is effective

over a wide range of incident angles up to  $50^\circ$  and can be well maintained at high temperature up to  $600^\circ\text{C}$ , which are useful in multi-angle and high temperature imaging applications. The proposed strategy here is shown to be mass-productive, tunable, simple and could be applied on curved substrates in principle. Moreover, by adopting modified etching parameters in fabricating process, pyramid structures with gradient effective refractive indices can also be fabricated by this strategy for wavelength non-selective IR window. In order to further facilitate the fabrication, conventional wet etching could also be tried. This strategy can also be extended to other IR materials and devices, such as Ge lens, IR cameras and IR photodetectors.

## Appendix

**Materials:** Analytical standard polystyrene (PS) and poly(methyl methacrylate) (PMMA) were purchased from the Sigma-Aldrich Co. Ltd. The Mw of PS and PMMA are 94900, 91500 respectively. Analytical reagent (AR) tetrahydrofuran (THF) (stabilized with 0.025% 2,6-di-tert-butyl-p-cresol), cyclohexane and acetic acid were purchased from Sinopharm Chemical Reagent Co., Ltd. These reagents were used as received. 2-inch and 4-inch double side polished Si wafers ( $R > 10000\ \text{ohm}\cdot\text{cm}$ ,  $\langle 100 \rangle / \langle 110 \rangle \langle 110 \rangle$ ) with a thickness of 0.5 mm were purchased from Hefei KeJing Materials Technology Co. Ltd and they were pre-cleaned using standard cleaning procedure before being delivered. Chromium (Cr) pieces for evaporation deposition were purchased from Kurt J. Lesker Company. Cr etchant was prepared by 21 ml AR perchloric acid, 100 g AR Ceric ammonium nitrate (Sinopharm Chemical Reagent Co., Ltd) and 500 ml deionized water.

**Fabrication of Subwavelength Structures:** PS (10 mg) and PMMA (10 mg) were firstly dissolved in THF (2 g) and ultrasound assisted fast dissolution was optional. Then certain amount (2 ml) of the polymer solution was taken by a dropper and spin-coated onto the pre-cleaned double side polished Si wafers. The solvent THF was evaporated in about ten seconds. The samples were immersed into acetic acid for 5 min to remove PMMA. 5 nm Cr was then deposited onto the above samples by electron beam evaporation system (Lab18, Kurt J. Lesker Company). The Cr/PS hybrid samples were immersed into cyclohexane to remove the PS phase and patterned Cr films were used as etching masks. Etching was performed by using the ICP-RIE technique (ICP 180, Oxford Plasmalab System100), Sulphur Hexafluoride ( $\text{SF}_6$ ) and Perfluorocyclobutane ( $\text{C}_4\text{F}_8$ ) were the etching gases. Parameters of RF power 30 W, ICP power 1200 W,  $\text{SF}_6$  25 sccm,  $\text{C}_4\text{F}_8$  50 sccm and varied etching duration time were used. Also, by changing the spin-coating speeds from 1000 rpm to 8000 rpm, varied masks with different characteristic lengths were prepared. Twelve mass ratios of PS to PMMA, 2.9:17.1, 3.3:16.7, 4:16, 5:15, 6.6:13.4, 7.5:12.5, 8.3:11.7, 10:10, 11.7:8.3, 12.5:7.5, 13.4:6.6 and 15:5, corresponding to molar ratios of 1:6, 1:5, 1:4, 1:3, 1:2, 1:1.7, 1:1.4, 1:1, 1.4:1, 1.7:1, 2:1 and 3:1, were used to obtain masks with different morphologies and filling factors. Finally, the etched samples were immersed into Cr etchant to remove Cr and rinsed using deionized water.

**Optical and Structural Characterization:** The microscopy images were taken by an optical microscope (Leica DM6000 M) connected with a CCD camera. The optical photographs were taken by a digital camera (Canon EOS 6D). The IR thermal images were taken by a IR thermal imaging camera (FLIR T420) with the spectral range of 7.5 to  $13\ \mu\text{m}$ . The microstructure images were characterized by field emission scanning electron microscopy (FESEM) (Zeiss Sigma 300). The thicknesses of polymer films were measured by a profilometer (Bruke Dektak XT).

**Spectra Measurement:** Transmission spectra of samples at normal incidence in the MIR region were measured by a Fourier-transform infrared spectrometer (FTIR) (Bruker Vertex 80v). The angle-resolved transmission spectra of samples were measured by the FTIR with the aid of a home-built rotatable accessory for placing the samples.

High temperature experiments: In order to simulate the actual high temperature application scenarios, the fabricated subwavelength structured samples and the commercial 3-5  $\mu\text{m}$  coated Si IR window (Edmund Optics, 68-524) were placed into an air muffle furnace (Sigma Instrument manufacture Co., LTD) and heated at 400  $^{\circ}\text{C}$ , 600  $^{\circ}\text{C}$ , 800  $^{\circ}\text{C}$ , 1000  $^{\circ}\text{C}$  respectively for 10 minutes.

More detailed results about our experiments are given in Figs. 8-15.

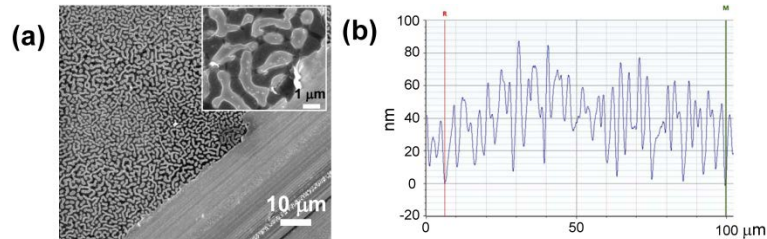


Fig. 8. (a) SEM images of the phase-separated PS pattern after scratching off a part for observing the film thickness. (b) Thickness curves of the phase-separated PS film measured by a profilometer.

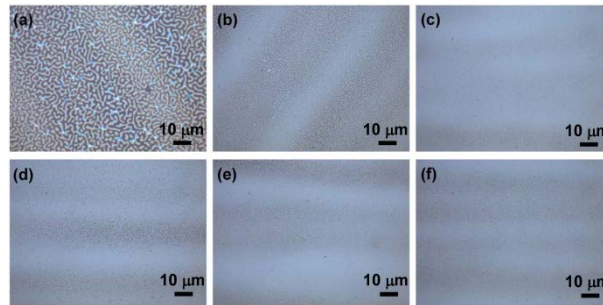


Fig. 9. (a)-(f) Optical microscopic images of the phase-separated PS patterns prepared with different spin-coating speeds: 1000 rpm, 2000 rpm, 3000 rpm, 6000 rpm, 7000 rpm and 8000 rpm.

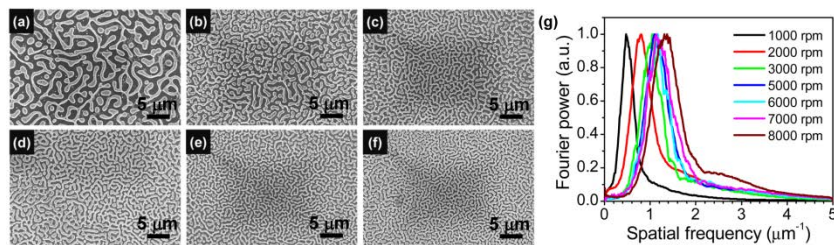


Fig. 10. (a)-(f) SEM images of Si subwavelength structures fabricated by using masks prepared at six different spin-coating speeds: (a) 1000 rpm, (b) 2000 rpm, (c) 3000 rpm, (d) 6000 rpm, (e) 7000 rpm and (f) 8000 rpm. (g) Rationally averaged Fourier transform spectra for the structures in (a)-(f). The molar ratio of PS to PMMA 1:1 was used for these samples and the etching duration time was fixed at 1 min.

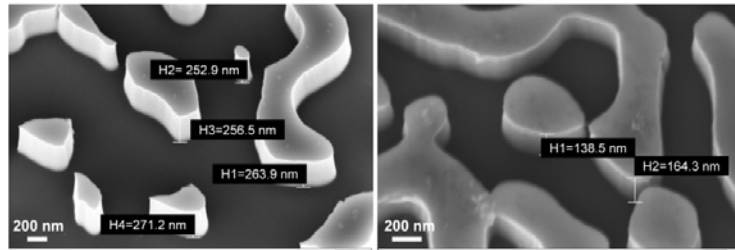


Fig. 11. Oblique SEM images of the samples fabricated by using masks prepared at two different spin-coating speeds (left: 3000 rpm, right: 7000 rpm).

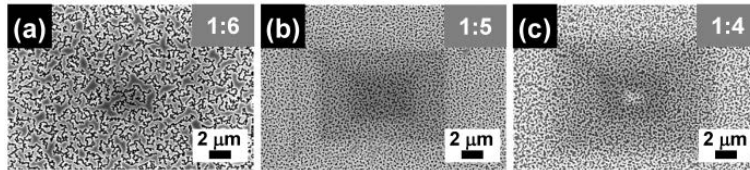


Fig. 12. (a)-(c) SEM images of the fabricated Si subwavelength structures by using masks prepared at molar ratios of PS to PMMA 1:6, 1:5 and 1:4. These samples have the same fabrication condition (spin-coating speed and etching duration time) with the samples in Figs. 5(a)-(h).

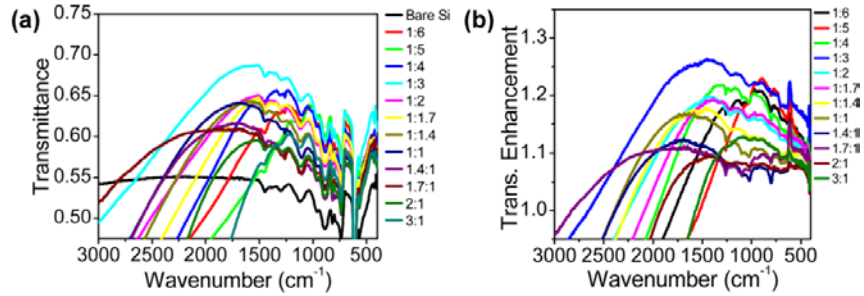


Fig. 13. (a) Measured transmission spectra and (b) transmission enhancement spectra for the fabricated subwavelength structured samples in Fig. 5.

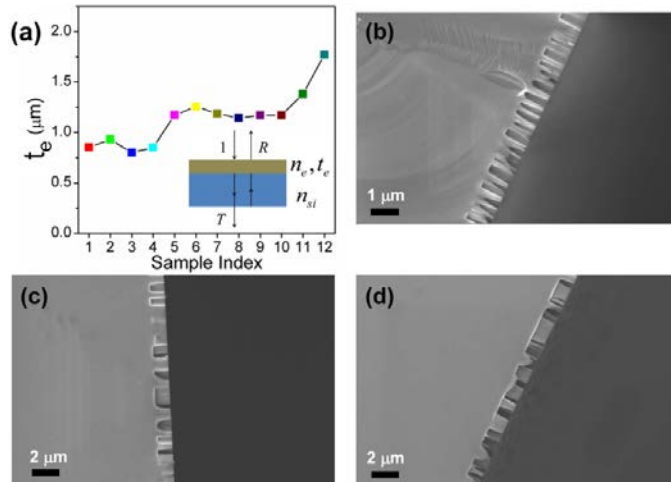


Fig. 14. (a) The thicknesses retrieved for twelve samples. Sample markers 1-12 represent the samples fabricated with molar ratios of PS to PMMA of 1:6, 1:5, 1:4, 1:3, 1:2, 1:1.7, 1:1.4, 1:1, 1.4:1, 1.7:1, 2:1, 3:1, respectively. (b)-(d) Cross-sectional SEM images of the samples fabricated with molar ratios of PS to PMMA 1:3, 1:1 and 2:1, respectively.

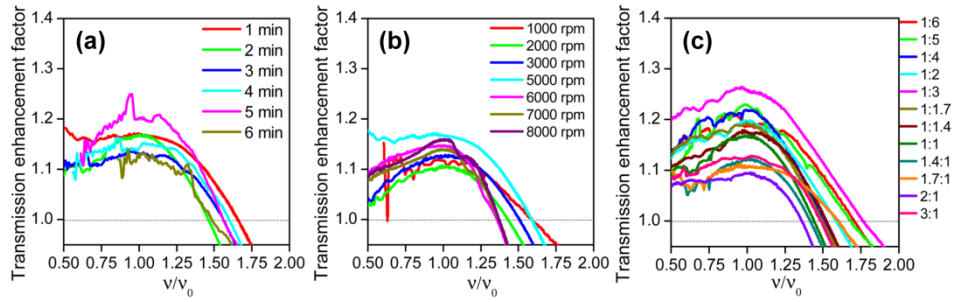


Fig. 15. (a) Enhanced transmission spectrum for Fig. 2(f) replotted with the wavenumber renormalized by the wavenumbers of transmission peaks.  $\nu$  is the wavenumber and  $\nu_0$  is the wavenumber of transmission peak. (b) and (c) are the same as (a), but for Fig. 3(f) and Fig. 5(i), respectively.

## Part II. Reflection and transmission through a Si wafer coated with a low-refractive-index layer

We consider a silicon slab with a refractive index  $n_{Si}$  and thickness  $t_{Si}$  ( $n_{Si}t_{Si} \gg \lambda$  with  $\lambda$  being the wavelength), which is coated by a dielectric film with a thickness  $t_e$  and refractive index  $n_e$  [inset in Fig. 14(a) in the Appendix]. For normal incidence of light upon the structure, the reflectance  $R$  and transmittance  $T$  can be derived as

$$R = R_1 + \frac{T_1^2 R_2}{1 - R_1 R_2}, \quad T = \frac{T_1 T_2}{1 - R_1 R_2}. \quad (1)$$

Here,  $R_1$  and  $T_1$  are the reflectance and transmittance for a semi-infinite Si substrate coated by a dielectric film with a thickness  $t_e$  and refractive index  $n_e$  at normal incidence, namely

$$R_1 = \frac{T_1}{4n_{Si}} \left| (1 - n_{Si})C + i(n_e - \frac{n_{Si}}{n_e})S \right|^2, \quad T_1 = 4n_{Si} \left| (1 + n_{Si})C - i(n_e + \frac{n_{Si}}{n_e})S \right|^{-2}. \quad (2)$$

where  $C = \cos p$ ,  $S = \sin p$ ,  $p = \frac{2\pi n_e t_e}{\lambda}$  [49], and the value of  $n_{Si}$  is taken from experimental data [50].  $R_2$  and  $T_2$  are the reflectance and transmittance for a semi-infinite Si substrate in air at normal incidence, namely

$$R_2 = \left( \frac{1 - n_{Si}}{1 + n_{Si}} \right)^2, \quad T_2 = \frac{4n_{Si}}{(1 + n_{Si})^2}. \quad (3)$$

We note that the light interference is considered in Eq. (2).

We consider the experimental situation that the incident light is coherent in thin structures, which gives rise to Eq. (2). However, the light interference does not occur in the thick Si slab ( $n_{Si}t_{Si} \gg \lambda$ ). Hence, a transfer-matrix method [51] with intensity vectors is applied to derive Eq. (1). Similar results have also been present in [52].

Then, the relationship between the transmittance enhancement and  $n_e$  can be obtained from Eq. (1), as shown as the black curve in Fig. 5(j).

## Funding

National Natural Science Foundation of China (11604355, 61521005, 11427807, 61422504, 11574037, 11774063, 11727811); Program 973 (2015CB659400); China National Key Basic Research Program (2016YFA0301100 and 2016YFA0302000).